Title: Shaking Table Tests and Numerical Analyses on a Scaled Dry-Joint Arch Undergoing Windowed Sine Pulses

Angelo Gaetani[a],[*], Paulo B. Lourenço[b], Giorgio Monti[c], Monica Moroni[d]

[a] Postdoctoral Research Fellow, Department of Structural Engineering and Geotechnics, Sapienza University of Rome, Faculty of Engineering, 00184 Rome, Italy. Phone: +39 0644585405; Fax: +39 064884852; E-mail: angelo.gaetani@uniroma1.it
[b] Full Professor, ISISE, Department of Civil Engineering, University of Minho, Campus de Azurem, 4800-058, Guimarães, Portugal. Phone: +351 253510209; Fax: +351 253510217; E-mail: pbl@civil.uminho.pt
[c] Full Professor, Department of Structural Engineering and Geotechnics, Sapienza University of Rome, Faculty of Architecture, 00197 Rome, Italy. Phone: +39 0649919197; Fax: +39 0649919150; E-mail: giorgio.monti@uniroma1.it
[d] Technician, Department of Civil and Environmental Engineering, Sapienza University of Rome, Faculty of Engineering, 00184 Rome, Italy. Phone: +39 0644585638; Fax: +39 0644585094; E-mail: monica.moroni@uniroma1.it

* Corresponding author

Abstract: The damages occurred during recent seismic events have emphasised the vulnerability of vaulted masonry structures, one of the most representative elements of worldwide cultural heritage. Although a certain consensus has been reached regarding the static behaviour of masonry arches, still more efforts are requested to investigate their dynamic behaviour. In this regard, the present paper aims to investigate the performance of a scaled dry-joint arch undergoing windowed sine pulses. A feature tracking based measuring technique was employed to evaluate the displacement of selected points, shading light on the failure mechanisms and gathering data for the calibration of the numerical model. This was built according to a micro-modelling approach of the finite element method, with voussoirs assumed very stiff and friction interface elements. Comparisons with existing literature are also stressed, together with comments about scale effects.

Keywords: dry-joint arch, seismic behaviour, masonry vaults, windowed sine pulse, tracking motion

1. Introduction

Unreinforced masonry vaults are diffused all over the world with more than six thousand years of history, with a religious and political symbolism that have likewise developed over time. Whereas, on the one hand, this long-lasting history clearly proves the adequacy of the past design processes to withstand gravitational loads, on the other hand, vaulted structures seem severely threatened by seismic events. The systematic observation of post-earthquake damages performed by the Italian Civil Defence Agency (National Civil Protection Service 2013) underlined the seismic vulnerability of vaulted structures and the consequent loss in terms of cultural, emotional and economic values, in addition to human lives.

Despite the great deal of research devoted to the static analysis of vaulted structures, studies on their dynamic behaviour are still rather limited, mainly focusing on rigid bodies dynamics (masonry elements as an assembly of dry-joint units). Starting with the pioneering work of Housner (1963), it is only thirty years later that the study of the rocking masonry arch was tackled by Oppenheim (1992). Under horizontal pulse excitation, the arch was considered as a rigid body four-link SDOF (single degree of freedom) mechanism, where the location of the four hinges (arranged in an alternating manner between intrados and extrados) was suitably assessed through a static equivalent analysis (**Fig. 1**a). Considering the nonlinear equation of motion for the SDOF mechanism, two cases were contemplated: 1) the arch fails after large rotations of the blocks or 2) the arch is safe if it is able to return to the rest position (**Fig. 1**b), that is, without investigating the post-impact behaviour (**Fig. 1**c). The same approach was followed by Clemente (1998) regarding the performance of stone arches under free vibrations (following an initial displacement), rectangular pulse and sinusoidal base acceleration.
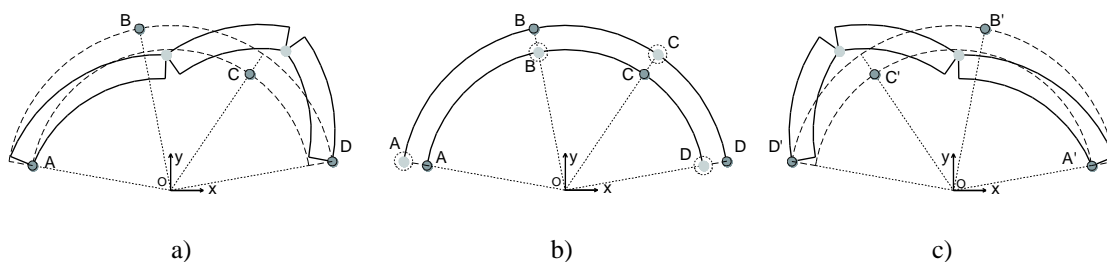

Fig. 1 The SDOF mechanism for an arch under base excitation: a) first half cycle, b) recovering and impact, c) second half cycle

Only recently DeJong and Ochsendorf (2006) stressed the importance of the post-impact behaviour. According to Discrete Element Method (DEM) analyses, the authors observed how the arch failure after the impact occurrence (**Fig. 1**c) represents the most critical configuration. Paralleling the results of Zhang and Makris (2001), DeJong and Ochsendorf (2006) referred to this type of failure as Mode 2, in contrast with Mode 1, that is, without

any impact. Zhang and Makris (2001) underlined also how rigid bodies are more vulnerable to a one-sine than a one-cosine impulse.

With the aim of improving Oppenheim's work, De Lorenzis et al. (2007) proposed a simplified analytical formulation to account for the behaviour of the arch after the impact, which makes the hinge location to flip in the symmetric position with respect the vertical axis of symmetry of the undeformed arch. The initial conditions for the post-impact behaviour (five unknowns) were calculated considering the coefficient of restitution that relates the rotational velocity (and, analogously, the kinetic energy) pre- and post-impact. This coefficient was found to be dependent only on the geometry of the arch and the number of voussoirs, and not on scale. Finally, the rocking behaviour was assumed to keep going back and forth until failure occurrence or until the arch returns to the rest position. Compared with DEM analyses and laboratory evidences (DeJong and Ochsendorf 2006; DeJong et al. 2008), the model proposed by De Lorenzis et al. (2007) appreciably matched the dynamic behaviour of the arch. However, the assumption of fixed hinge location (pre- and post-impact) and the neglect of sliding between blocks are limitations of the model.

On the basis of the previous work, considering the response of the analytical model for a range of impulse accelerations and periods, DeJong et al. (2008) proposed a regression equation fitted on the failure cases for a one-cycle sine pulse. The numerical results were compared with shaking table tests on two scaled dry-joint arches built with autoclaved aerated concrete blocks. In particular, beside a tilting test, five time histories of real earthquakes and harmonic signals were implemented. Moreover, considering the analytical description of the dynamic behaviour of the arch, DeJong and Dimitrakopoulos (2014) proposed a methodology to derive approximate equivalence between the single rocking block and arch rocking mechanisms through local linearization of the equations of motion. In particular, the authors underlined the analogy between the arch and the asymmetric rocking frame, both of them activating a three-block mechanism.

Regarding pure numerical analyses, beside limit analysis calculation (Clemente 1997; De Luca et al. 2004; Drosopoulos et al. 2006; Monti et al. 2013; Dimitri and Tornabene 2015; da Porto et al. 2016; Tecchio et al. 2016), as already stressed, DEM seems well suited for the analysis of historical stone masonry structures under earthquakes. Variations of the method are usually designated by UDEC, NSCD and DDA, Universal Distinct Element Code, Non-Smooth Contact Dynamics, and Discrete Deformation Analysis, respectively. The principal contributions for the analysis of arched structures are: UDEC (Lemos 1998; Tóth et al. 2009; Dimitri et al. 2011; Dimitri and Tornabene 2015); NSCD (Rafiee et al. 2008; Albuerne et al. 2013; Rafiee and Vinches 2013; Lancioni

et al. 2016); DDA (Pérez-Aparicio et al. 2013). Thavalingam et al. (2001), instead, performed a comparison between DDA, DEM based Particle Flow Code and a non-linear finite element (FEM).

Considering FEM methods, by means of fibre beam approach, De Santis and de Felice (2014) performed nonlinear static and dynamic analyses on masonry arches of different geometrical and mechanical properties. Also Pelà et al. (2009) performed nonlinear static analyses, calibrating the mechanical parameters and the restraint conditions according to recorded vibration frequencies and modal shapes, together with the Drucker-Prager failure criterion. Milani and Lourenço (2012) proposed a 3D numerical model for the analysis of masonry bridges interacting with the backfill. Compared with DEM and the Applied Element Method AEM, the non-commercial software developed by the authors showed a better description of the arch behaviour.

On the other hand, many researchers have recently performed dynamic tests on arched structures. Calderini et al. (2015) investigated the behaviour of an arch-pillars system pre- and post-strengthening by the use of tie-rods. Giamundo and co-workers (2015; 2016) carried out an experimental campaign regarding the performance of a barrel vault before and after the application of an inorganic matrix composite grid reinforcement.

From the above considerations, the present contribution is aimed at investigating in detail the behaviour of a masonry arch to simple pulses, to which rigid block structures result more vulnerable (Zhang and Makris 2001; Kalkan and Kunnath 2006; DeJong et al. 2008; DeJong and Dimitrakopoulos 2014). In this regard, as a certain consensus has been reached for one-cycle sine pulse with at rest initial conditions, the study of a dry-joint scaled arch undergoing a windowed three-cycle sine pulse signal is here presented. Besides the fact that the main pulse occurs with not at rest initial conditions, no clear assumptions can be made on the location of the hinges throughout the test. Therefore, the adopted signal eliminates one of the main limitations of similar tests described in the available literature. The numerical simulation of the tests is also described. Transient analyses through FEM micro-modelling have been performed, providing a contribution for the definition of joint properties.

Regarding the experimental setup, a scaled arch assembled by dry-joint 3D printed voussoirs was built and tested on a shaking table. All the results have been plotted in frequency-amplitude domain, allowing estimating a failure curve in accordance with similar results available in literature. The in-plane motion of the arch was recorded with a tracking motion system, in the fashion of (Albuerne and Williams 2015; Calderini and Lagomarsino 2015; Calderini et al. 2015). The tests were carried out in the Structures and Materials Laboratory in Sapienza University of Rome, whereas the image analysis technique was developed at the Hydraulics Laboratory of the same University.

On the other hand, the numerical simulations have been carried out through a commercially available FEM software, namely DIANA (TNO DIANA BV 2014). Although several studies have been carried out on masonry elements in this field, mostly walls, the application of FEM micro-modelling on vaulted structures seems still limited (Lourenço et al. 2010; Milani and Lourenço 2012; Ptaszkowska and Oliveira 2014; Rossi et al. 2014), even less in case of dynamic analysis (Liberatore et al. 1997). In this regard, a sensitivity analysis on the normal and tangential stiffness is presented, together with considerations on damping. Finally, scale effects are discussed.

2. Test setup

2.1 Geometry

The geometrical features of the tested arch are reported in Fig. **2**, where the arch has an angle of embrace of 140°, it is 92 mm wide, and the inclined supports were realized with steel angle bars bolted to the platform. Regarding the base, it is a magnesium slip table 700 x 700 mm^2 large and 45 mm thick connected to an electrical-dynamic shaker with V-shaped guide rail. In order to tune the drive signal sent to the slip table, ceramic shear accelerometers were used.

Regarding the blocks, these were printed according to Fused Deposition Modelling technology with up to 0.1 mm accuracy. The constituting material was the Acrylonitrile Butadiene Styrene (ABS), which is a widely used thermoplastic material. Moreover, in order to achieve the same friction coefficient as masonry elements, a mixture of fine sand (0.2 ÷ 1.0 mm diameter grain size) and polyester bi-component resin was spread on the lateral surface of the blocks, reaching an average value of 0.68 (friction angle equal to 34°). The mixture bonded well to the plastic surface of the blocks without showing a significant deterioration along the test campaign. The same mixture was applied to the supports to guarantee a consistent behaviour.

Finally, since the material properties of the blocks, namely mass density, elasticity, strength, etc., do not affect the problem (at least in the linear range), only the external frame of the voussoirs was printed, filling the inner part with wood inserts. Considering the resulting mass density equal to around 450 kg/m^3, the total mass of the specimen was 1.4 kg. The steel supports weight 1.7 kg each.
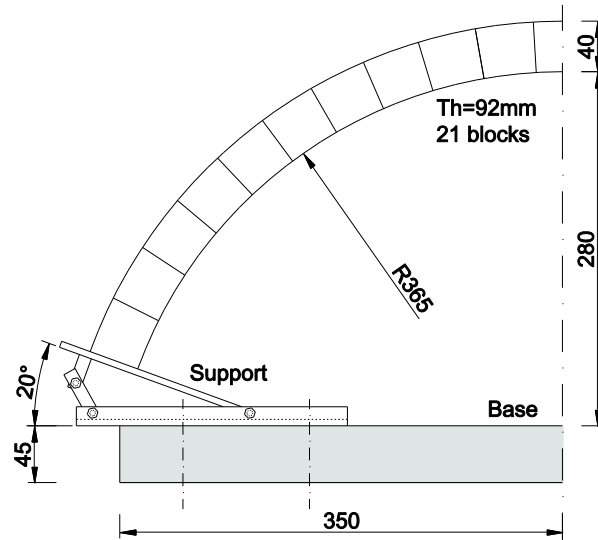
Fig. 2 Geometrical dimensions of the tested arch

2.2 Feature tracking based measuring technique

According to **Fig. 3**, reference data were provided by an acquisition system consisting of: 1) a high-speed, high-resolution camera (Mikrotron EoSens) equipped with a 50-mm focal length lens capturing grey-scale images at up to 500 fps with a resolution of 1280×1024 pixels (for the present set of measurements, images were acquired at 400 fps); 2) a high-speed Camera Link digital video recorder operating in Full configuration (IO Industries DVR Express Core) to manage data acquisition and storage. The captured images were transferred to a personal computer under the control of the Express Core software. The images acquired by the Mikrotron EoSens camera were processed using a Lagrangian Particle Tracking technique named Hybrid Lagrangian Particle Tracking (HLPT) (Shindler et al. 2012). HLPT selects image features (image portions suitable to be tracked because their luminosity remains almost unchanged for small time intervals), determines the centroids of the particle associated to the features and tracks these from frame to frame. Though HLPT was developed to process images from fluid mechanics experiments (Moroni and Cenedese 2015), it was successfully employed here to track the markers on the voussoirs undergoing the motion. Feature detection within the HLPT algorithm is based on the solution of the Optical Flow (OF) equation, which defines the conservation of the pixel brightness intensity among couples of images. Since the OF equation is insufficient to compute the two unknown in-plane velocity components associated to each pixel, the equation is computed in a window $W=H{\times}V$ (where H and V are the horizontal and vertical dimensions of the window respectively) centred at the pixel location. The OF equation is solved for a limited number of image pixels. Those pixels, named features, are determined by inverting the Harris matrix, defined only by the image grey levels (Shindler et al. 2012). Once the features are identified, two 1D Gaussian

functions built around the integer position of each detected feature are used to compute the centroid coordinates. To track the centroids, the "Sum of Squared Differences" (SSD) among intensity values is used as the matching measure. The SSD was computed considering a centroid (and its interrogation window) and its "most similar" region at the successive time. The displacement is thus defined as the one that minimizes the SSD (Moroni and Cenedese 2005). Once the trajectories are reconstructed, displacement, velocity, and acceleration vectors are computed via central differences.
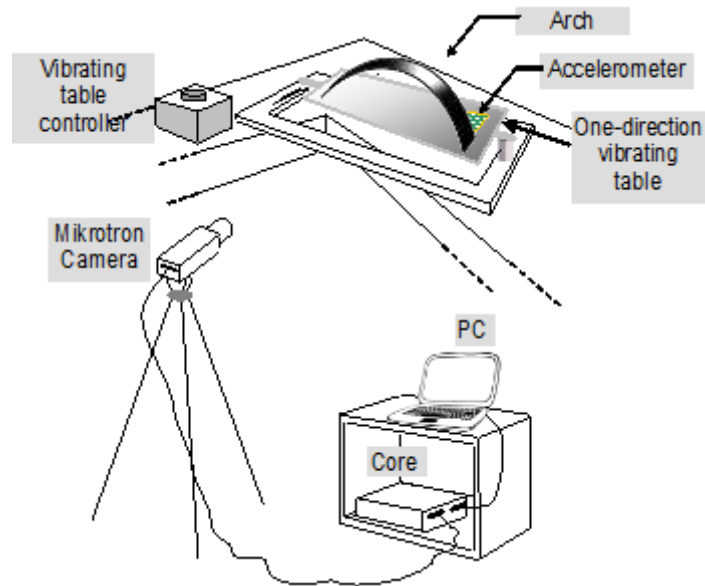

Fig. 3 Experimental setup

3. Laboratory experiments

3.1 Tilting tests

Tilting test represents a first order seismic assessment method and consists in a quasi-static rotation of the base platform until structure failure occurs. From the mechanical point of view, this test assumes a constant horizontal acceleration of infinite duration. Therefore, the dynamic behaviour of the structure is neglected and the consequent arch stability assessment may be excessively conservative. In this regard, it is well-known that the horizontal acceleration that activates the SDOF mechanism, i.e. the formation of four hinges, is smaller than the collapsing one. Rigid bodies, in fact, can move back to the rest position if the seismic impulse duration or the energy content are not large enough, or if no other impulses increase the oscillations (Clemente 1998; De Lorenzis et al. 2007; Dimitri et al. 2011). However, tilting tests are still valuable in providing an accurate assessment of the collapse mechanism and the lower bound seismic capacity.

It is worth noting that, in the local reference, tilting the model implies that the vertical acceleration reduces in magnitude as the horizontal acceleration increases. Even so, since the problem is purely based on the stability and not on the stresses within the structure, this becomes a non-issue. The goal is thus only the ratio between horizontal and vertical acceleration, which is basically the tangent of the angle of tilt.

In order to account for possible imperfections due to the manual assembling, the test was performed three times providing an average horizontal load multiplier $\lambda = 0.29$, which can be addressed as the fraction of the gravity acceleration necessary to transform the arch in a SDOF mechanism. **Fig. 4**a reports the schematic view of the SDOF mechanism (where the hinge location is identified by central angles), whereas Fig. **4**b shows the frame of the collapsing arch during the test.
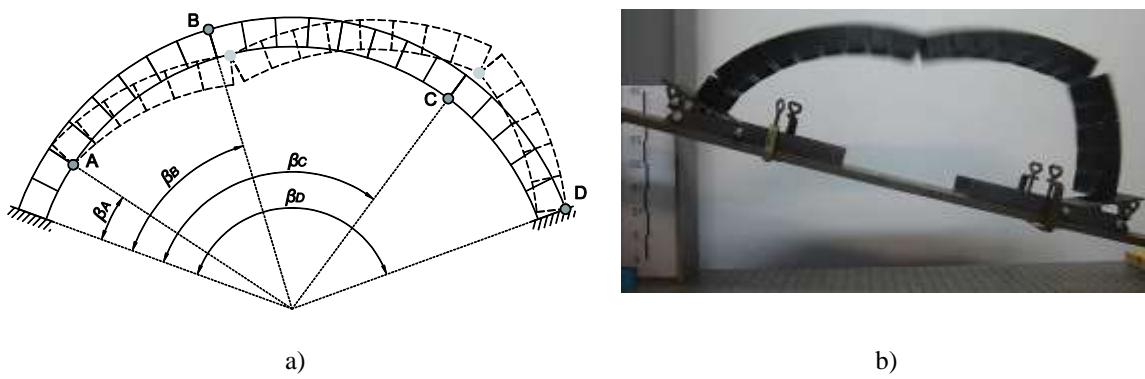

a)   b)

Fig. 4 Arch mechanism following horizontal actions: a) schematic view and b) frame of the tilting test

3.2 Shaking table tests

The experimental campaign was aimed at evaluating the dynamic behaviour of the arch undergoing a series of one-cycle sine impulses with different amplitude and frequency. However, in order to meet the features of the equipment used to perform the tests, the signal was first windowed. The shaking table adopted for the dynamic tests, in fact, is based on an electrical-dynamic vibration system, that is, the circulation of current in the armature produces a magnetic field, thus the acceleration of the table. Accordingly, since no current circulates at the end of the tests, the table eventually returns to the rest position, i.e. null displacement and velocity. In order to address this aspect, the sine-shaped pulse was windowed by a Bohman window. Moreover, considering that the windowing process mainly affects the initial and final part of the signal, three cycles of sine were implemented, ensuring thus a unique central impulse. As an example, considering a 1.3 g, 10 Hz three-cycle sine signal, the effects of the windowing are reported in **Fig. 5**. As it is possible to see, the un-windowed acceleration produces a conspicuously large residual displacement (for the sake of clarity, the plot is stopped at the end of the first cycle). Also the

velocities have different magnitude but, on the contrary, the accelerations of the two inputs are rather similar in the central part of the signal.
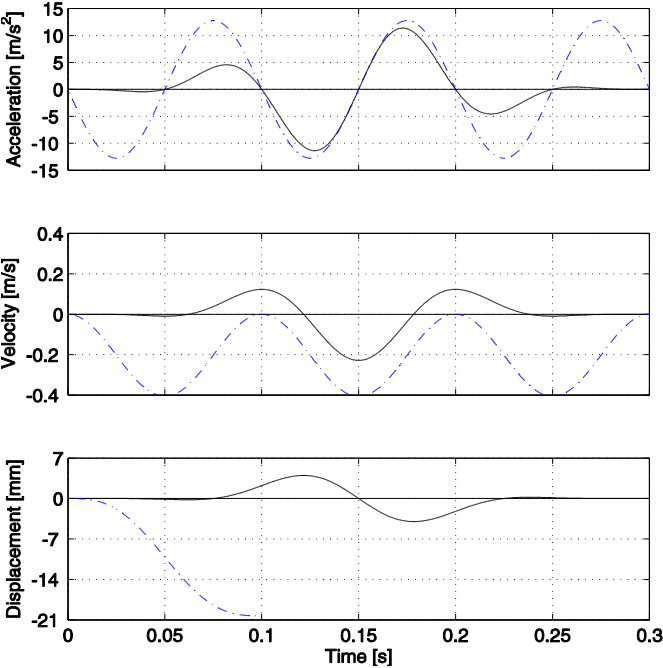

Fig. 5 1.3 g, 10 Hz pre- and post-windowed signal (dash-dot blue line and black solid line, respectively)

Considering the same signal, the comparison between the input acceleration history (i.e. drive) and the acceleration time history recorded on the table is reported in **Fig. 6**. The comparison is extended to velocity and displacement, as single and double integration of the acceleration. As it is possible to see, the output signal matched almost perfectly the input one for what concerns the frequency, but the peak acceleration is slightly larger for the recorded one. Moreover, the acceleration graph shows minor parts with high frequency acceleration, due to small impacts of the table in the change of directions. Given their short duration, they are not expected to modify the final results. In this regard, De Lorenzis et al. (2007) state that at high frequencies an arch does not fail by hinging and rocking, but it may fail due to long-lasting vibration between the voussoirs.
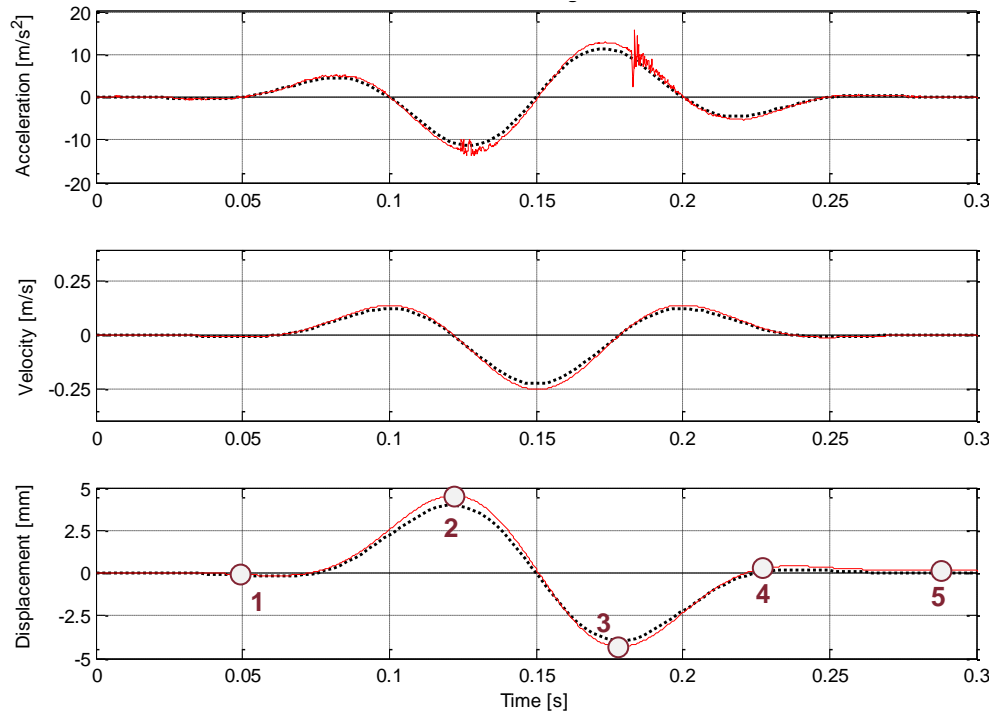
Fig. 6 1.3 g, 10 Hz signal: comparison between input signal (drive) and recorded signal (dot black line and red solid line, respectively)

Given the possible assembling imperfections, each test was repeated three times. Frequency and amplitude were increased progressively until at least two collapses were registered, out of the three repetitions. A total of 69 runs was performed and the results are collected in **Fig. 7**, together with the outcome of the tilting test ($\lambda = 0.29$). Since the quasi-static nature of the latter, this represents the expected asymptote (in the lower frequency range) of any dynamic test campaign. By extension, the horizontal load multiplier provided by the tilting test denotes the threshold of the region where impulses cause no hinge to form, i.e. the arch acts as a rigid body following the base motion (DeJong et al. 2008). In general, the comparison between dynamic and tilting tests highlights how much a quasi-static analysis may underestimate the capacity of the arch.

On the other hand, in order to highlight the trend of the dynamic tests, a linear regression analysis was performed (after a logarithmic transformation of the data) as an interpolation of the failure inputs. This allowed calculating an exponential curve (red dot line) constrained to asymptotically reach (for lower frequencies) the value provided by the tilting test. As it is possible to observe in **Fig. 7**, the fitted line matches well the results, with a coefficient of determination equal to $R^2 = 0.98$. Considering f_p and a_p as the frequency and impulse amplitude, respectively, Equation (1) reports the regression equation:

$$a_p = 0.0647e^{0.2801f_p} + 0.225 \tag{1}$$

By extension, this failure curve may be assumed as a threshold for stability condition: the area below the curve indicates safe inputs, whereas the area over it indicates collapse inputs.

The results of the experimental campaign were also compared with the curve computed according to DeJong et al. (2008, Table 3, with $\lambda = 0.30$, $C_1 = 0.02$, $C_2 = -0.81$, and $t_{min} = 0.11$), which represents the failure curve for the arch with 10% reduction thickness (as discussed in Section 4.1 below) undergoing a one-cycle sine impulse. As it is possible to notice, the latter curve is considerably more conservative and the reason lies on the out-of-phase impulses of the windowed signal implemented here. According to Clemente (1998), the tested arch would have failed due to unsafe rotations if additional impulses had not restored the displacements in a safety range. For this reason, compared to the one-cycle sine impulse, the arch showed a larger capacity, that is, the frequency being equal, the arch stood overall larger amplitude accelerations.
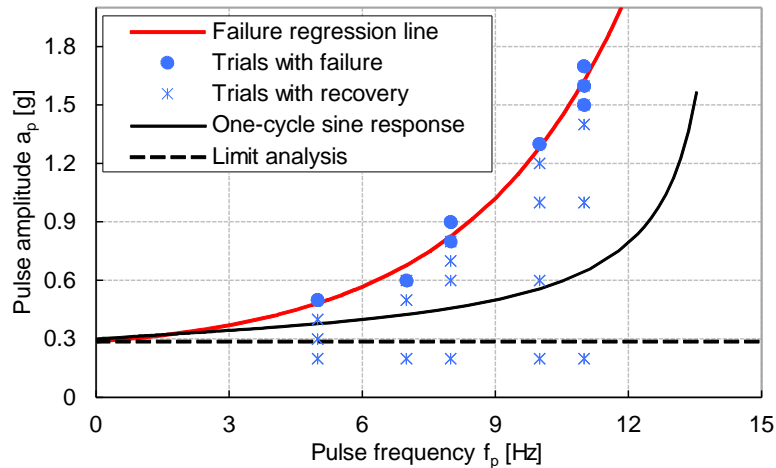

Fig. 7 Results of the shaking table tests

The arch usually failed after the end of the input signal following an apparent chaotic alternating four-hinge mechanism without experiencing any sliding between the blocks (due to the slenderness of the arch). In this regard, the numerical analyses performed by De Lorenzis et al. (2007) showed how, for a one-cycle sine impulse, hinge locations may change several times within a single half cycle of motion. In the present case, the behaviour observed was similar but more severe: additional hinges occurred when a clear four-hinge mechanisms was interrupted by further impulses out-of-phase with the rocking motion (DeJong et al. 2008). Accordingly, the arch may even (temporarily) experience larger and unsafe rotations if the subsequent impulse restores the displacements in a safety range (Clemente 1998). Considering the signal implemented in the present investigation (**Fig. 5**), the fade-

in phase de-amplified the response for the specific pulse considered but, in general, initial conditions can either amplify or de-amplify the response (DeJong and Ochsendorf 2010; DeJong 2012).

Focusing only on the trials with failure, a certain trend in the behaviour of the arch was detected. Considering, for instance, the time history reported in **Fig. 5** and **Fig. 6**, the central part of the displacement graph resembles a one-cycle sinusoidal wave. In particular, looking at **Fig. 6**, three main movements (phases) can be detected: 1-2, forward from rest position to the positive peak; 2-3, reverse movement, until the negative peak; 3-4, again forward movement; 4-5, slowly back to the rest position.

The visual inspection of the recorded videos showed that several features were persistent in the tests. In particular, the phase 1-2 produced a clear movement of the arch with a rather limited hinge opening. In particular, following the outcome of the tilting test, only an acceleration larger than 0.29 g can activate a mechanism. Consequently, with reference to **Fig. 6**, being the amplitude of the first lobe almost equal to half of the main pulse one, all pulses reported in **Fig. 7** with amplitude larger than 0.7 g made the arch rock before the main pulse occurrence. During the subsequent phase 2-3, the previous displacement reversed developing a clear four-hinge mechanism in accordance to the tilting test (compare full circles of **Fig. 8** and **Fig. 4**a). The phase 3-4, completely out-of-phase, led to a more chaotic behaviour, with even a temporary occurrence of a fifth hinge and a sort of migration of the already open hinges. This migration is schematized with arrows in **Fig. 8**, together with the final four-hinge configuration reached during 4-5. Hinges C and D kept opening until the failure occurrence. In the case of one-cycle sine impulse, for which the most critical failure mode is consequent to a clear flipping impact which mirrors the primary mechanism. Conversely, in the present case the kinematics of the arch is mainly determined by a smooth progression of the hinge location, ending up with an unexpected failure configuration.
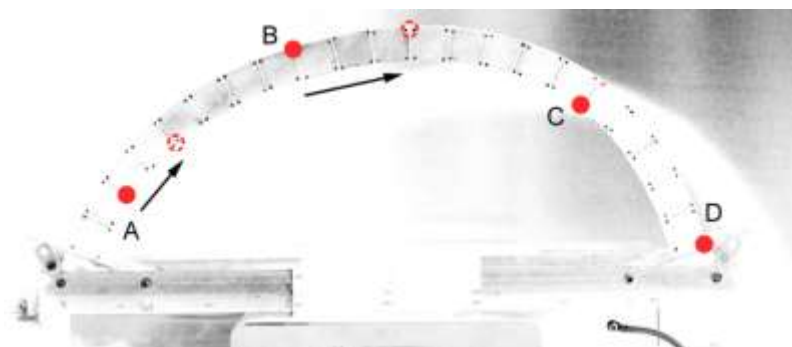

Fig. 8 Schematic description of initial (full circles) and final hinge location (dashed line). Hinges C and D do not experience significant change of location, and coincide in full and dashed circles.

4. Numerical analyses

4.1 Limit analysis

Corner rounding, slight variations in block size and imperfections in the manually assembled geometry may lead to a not accurate match of the voussoir lateral surfaces or a not perfect semi-circular shape, resulting in an overall reduction of the arch capacity. In order to account for this aspect, DeJong et al. (2008) suggested to consider a numerical model with a 20% reduction in the arch thickness (10 ÷ 15% due to corner rounding and 5 ÷ 10% due to slight variations in thickness and imperfections in the constructed geometry). The same approach was pursued by Albuerne et al. (2013), whose numerical model overestimated the capacity of the tested arch by approximately 25%. In order to tune the numerical model with the experimental evidence, the latter authors considered a reduced thickness equal to 82% of the original value.

To evaluate this aspect, the preliminary results provided by tilting analysis were compared with literature. In this regard, Clemente (1997) and Alexakis and Makris (2014) performed parametric limit analyses considering the principle of virtual works and a variational formulation, respectively, achieving very similar results. The authors estimated the horizontal load multiplier λ and the position of the hinges simply according to the thickness/centreline radius ratio (th/R) and angle of embrace β. Considering the geometrical data of the tested arch (**Fig. 2**), the comparison led to a reduction of the thickness for the numerical model of 10%, that is, maintaining the same centerline radius, $th/R = 36/375 = 0.096$. According to literature, the theoretical multiplier is $\lambda = 0.30$, 3% larger than the experimental one ($\lambda = 0.29$). The comparison interested also the hinge locations showing a good agreement between the experimental and the expected results.

4.2 Nonlinear static analyses

The numerical analyses have been carried out through a commercial FEM software, namely DIANA (TNO DIANA BV 2014), considering very stiff and infinitely resistant voussoirs (Young modulus E = 10^5 MPa), with friction interface elements. In particular, a Coulomb friction interface has been adopted with cohesion, tensile strength and dilatancy angle set to zero. The friction angle was assumed 34° and the mass density equal to 450 kg/m^3, as measures in experiments. On the other hand, interface stiffness plays, unexpectedly, a role of capital importance. Given the peculiarity of the material adopted and the overall low stress levels expected during the tests, the interface stiffness was assessed by means of a sensitivity analysis on the final results. The range of value was deduced from literature, for both FEM and DEM analyses (Lourenço 1996; Tóth et al. 2009; Senthivel and Lourenço 2009; Lourenço et al. 2010; Dimitri et al. 2011; Ptaszkowska and Oliveira 2014; Dimitri and Tornabene

2015; Giamundo et al. 2016). Moreover, with the aim of avoiding excessive block interpenetration, the limitation $K_n > 0.1$ N/mm^3 and $K_t > 0.04$ N/mm^3 (normal and tangential stiffness, respectively) have been assumed. The ratio between the two stiffness was set equal to 0.4 as the ratio between tangential and Young modulus with a Poisson's ratio equal to 0.2 (Senthivel and Lourenço 2009).

Attention was paid also to the geometrical nonlinearities. In order to account for them, rather than a Total Lagrange formulation (TL), which is more suitable for large rotations and displacements and small strains, an Updated Lagrange formulation (UL) was selected (TNO DIANA BV 2014). Since the deformation of the arch model is totally concentrated in the interface elements (exhibiting large displacements and strains), UL allowed a more advantageous framework for the description of large inelastic deformations.

The mesh was generated considering plane triangle elements (T18IF) for the interfaces and tetrahedral elements (TE12L) for the voussoirs. The choice of implementing a three-dimensional model for analysing a phenomenon that is basically in-plane is due to future extension of the present model to study masonry vaults with three-dimensional behaviour.

Since the voussoirs are assumed very stiff and infinitely resistant (whose behaviour is theoretically not affected by the FE discretization), in order to understand the effect of the mesh size in the description of the nonlinear behaviour of the interface elements, a mesh sensitivity analysis was performed. This is aimed at achieving an adequate balance between accuracy and computational effort, a crucial aspect for the subsequent analyses. The results of this study are reported in **Table 1**, where the comparison is limited to the multiplier of the horizontal load, as the mesh size does not significantly affect the failure mechanism. The failure mechanism, in particular, is in good agreement with tilting test and limit analysis.

As expected, the more refined is the mesh, the longer is the analysis, and the more accurate the results, almost coincident with the theoretical result provided by limit analysis (Clemente 1998). However, according to the goal of this study, the mesh with 32 elements, that is, four elements along the thickness, was considered adequate for the subsequent analyses since it led to less than 5% difference with respect to the limit analysis.

Interface elements	Load multiplier λ	Comparison with limit analysis (Clemente 1998)	Running time*
8	0.247	-17,7%	1 min
32	**0.286**	**-4,7%**	**>4 min**
128	0.296	-1,3%	>14 min
512	0.299	-0,3%	>105 min

* Intel Core i7-3820 (3.60 GHz), RAM: 16 GB, Disk: SSD disk

Table 1 Mesh sensitivity analysis considering the theoretical limit value $\lambda = 0.30$ (Clemente 1998)

On the other hand, in case UL is considered, taking the horizontal displacement of the keystone as control point, **Fig. 9** shows the capacity curves of the arch adopting three sets of interface stiffness. As it is possible to notice, the maximum capacity never reaches the one provided by the tilting analysis, unless large values of stiffness are considered. This behaviour can be ascribed to the normal stiffness of the interface. A small value inevitably leads to interpenetration of the voussoirs and the position of the hinge (supposed either at the intrados or at the extrados) to move inward, reducing the "effective" thickness of the arch (**Fig. 10**). This means the arch is basically thinner, thus with a lower capacity. In reverse, a hypothetical infinite interface stiffness would cause the hinges to locate on the edge line of the arch. In this regard, higher values of stiffness provide more suitable results. This effect can also justify the reduction of arch height proposed by several authors, as stated before and that the inverse problem of obtaining the "effective" thickness of dry-joint masonry arch needs to be addressed using force-displacements, and not only ultimate load.

Moreover, the softening branch of the curves clearly tends to a unique displacement (estimated equal to 6.6 mm), which can be regarded as the ultimate displacement of the arch. The envelope of all the curves can be approximated with a straight line, whose shape parallels the nonlinear kinematic capacity curve of a rigid block undergoing horizontal forces and rocking in the base. For further description on this topic, among others, the reader is referred to (Doherty et al. 2002; Griffith et al. 2003; Griffith et al. 2004; de Felice 2011; Al Shawa et al. 2012).
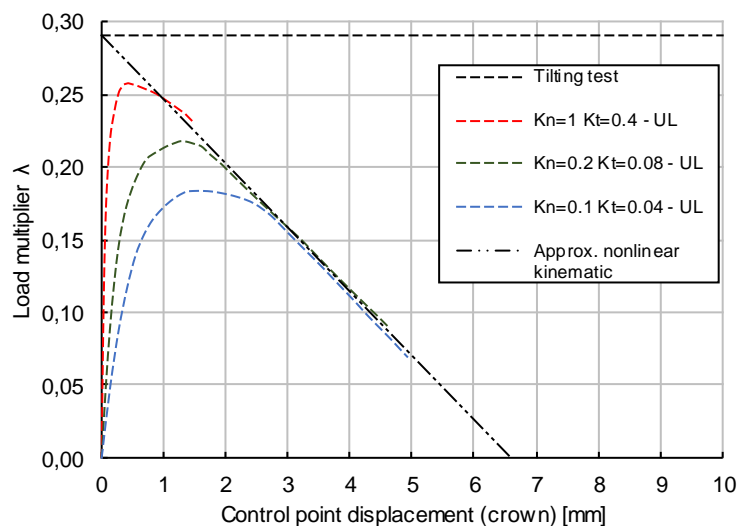

Fig. 9 Arch capacity curves varying the interface stiffness [N/mm^3], with geometrical nonlinearities UL

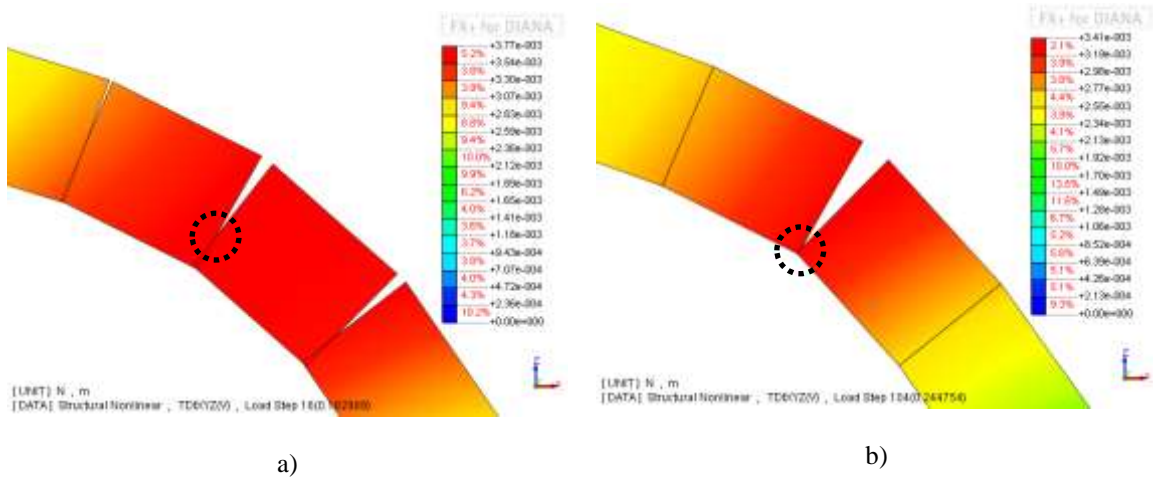**Fig. 10** Hinge location for: a) $K_n = K_t = 0.1$ N/mm^3, and b) $K_n = K_t = 10$ N/mm^3

4.3 Transient analysis

The accelerograms recorded on the slip table during the tests were filtered before being used as input for the numerical analyses. In particular, an elliptic-type low- and high-pass filter was adopted, maintaining only the range 1÷50 Hz. For instance, **Fig. 11** shows how the filtering process on the 1.3 g and 10 Hz signal got rid of the high-frequency content (see also **Fig. 6**). Moreover, UL was used in order to account for geometrical nonlinearities and this requested very small time step for the analysis to converge. In the present case, the step size was explicitly specified equal to 2×10^{-5} s. The equilibrium iteration method used for the steps was the Quasi-Newton (Secant) method based on BFGS algorithm (TNO DIANA BV 2014). The energy norm convergence criterion for the equilibrium iteration process was adopted with a tolerance of 1×10^{-3}.

Regarding the time integration scheme, the Hilber-Hughes-Taylor method (HHT, also called α-method) was adopted, being unconditionally stable if α = –1/3 ÷ 0. As far as numerical dissipation is concerned, given the integration step adopted in the present study, i.e. 2×10^{-5} s, its effects appear rather negligible. In particular, according to Hilber et al. (1977, Fig. 4), having chosen α = –0.1, the modes with frequency higher than 10000 Hz result with a damping ratio larger than 0.01. For further approaches to the study of dissipation for rigid block structures, the reader is referred to e.g. (Liberatore et al. 1997; Peña et al. 2006; DeJong 2009).

With respect to damping, the main difficulty is posed by the mathematical approximation. The most used approach is the viscous damping according to the Rayleigh formulation, but two key drawbacks must be stressed for dry-joint structures. Firstly, although for continuum modelling the damping is usually set equal to 5%, for rigid block dynamics there are no recommendations on its magnitude. For instance, in case of DEM analyses the values suggested in literature are at least one order of magnitude smaller (Peña et al. 2006; De Lorenzis et al. 2007).

Secondly, a rigorous approach for defining the damping parameters is still missing. In this regard, DeJong (2009) provided recommendations for calculating Rayleigh damping parameters for DEM analyses. According to the author, mass-proportional damping should be either extremely small or eliminated entirely, whereas the stiffness-proportional damping should be preserved to damp high frequencies out and get physically reasonable results.
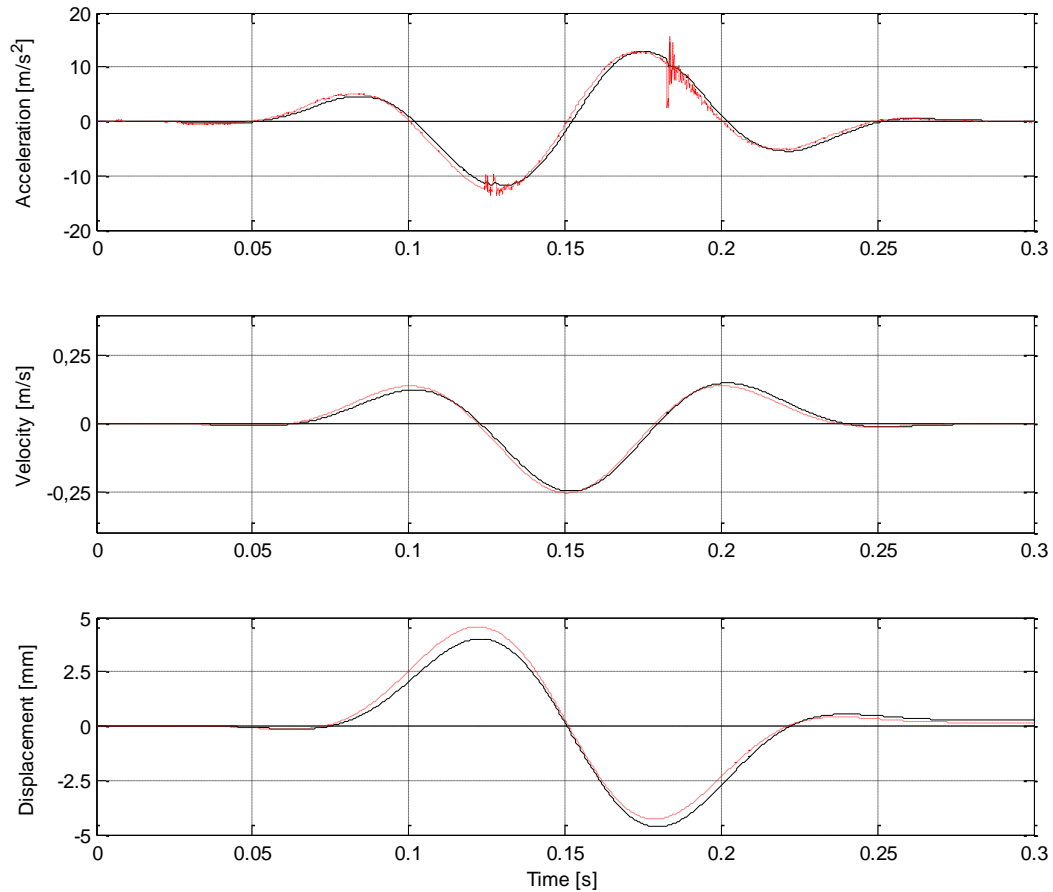

Fig. 11 Time history recorded on the slip table: pre- and post-filtering for the 1.3 g and 10 Hz signal

(red dot line and solid black line, respectively)

Structural damping represents another possible schematization of damping: It is independent of the frequency and proportional to the displacement, usually suggested in case local frictional effects are present throughout the model, such as dry rubbing of joints in a multi-link structure (TNO DIANA BV 2014). Since sliding phenomena were not evident in the tests and the present study is based on the stability of the arch (with large displacements), this form of damping can result in too conservative effects.

Therefore, considering that small impacts (the main source of energy dissipation) were detected during the tests (mostly involving the migration of hinges A and B, as shown in **Fig. 8**), and the very small values proposed

in literature for DEM analysis of dry-joint arches, in the present study, a null value of the Rayleigh damping ratio was adopted. Inelastic damping appears naturally in the structural model.

With the aim of validating the model against the experimental results, a sensitivity study regarding the interface stiffness was performed. Paralleling section 4.2, K_n was assumed equal to 0.01, 0.1, 1, 10, 100 N/mm^3, whereas K_t was assumed equal to 0.1, 0.4 and 1 times K_n, resulting thus in 15 different sets. Whereas on the one hand the value 0.4 represents the same ratio assumed for the nonlinear static analysis, on the other hand, the ratios 0.1 and 1 were considered as additional limit values. Stiffness values out of the proposed range were also adopted, leading to severe problems of convergence. This aspect is also stressed in literature. For instance, referring to the range of values adopted for performing DEM analyses ($5\times10^{11} \div 5\times10^{12}$ N/mm^3), De Lorenzis et al. (2007) stated that lower stiffness values can lead to contact overlap errors, whereas larger values can lead to excessively small time steps for the solution to remain stable.

Given the dependence of the displacements on the interface stiffness (as stressed in **Fig. 10**), the numerical analyses have been compared according to the deformed shape and hinge location. As far as the tangential stiffness is concerned, in case $K_t / K_n = 0.1$, sliding between blocks was evident, although not expected from both literature perspective (De Lorenzis et al. 2007; D'Ayala and Tomasoni 2011) and experimental evidences. On the other hand, the ratios 0.4 and 1 led to almost coincident results.

In order to provide a comparison between different sets of stiffness properties, **Fig. 13** shows the deformed shapes relative to the same instant (when a former mechanism is more evident) of several analyses for the 1.3 g and 10 Hz signal. The frame of the experimental test is also reported. Besides the magnitude of the displacements, the comparison shows how the interface stiffness strongly influences the mechanism. Looking at hinge locations (highlighted in the first frame), increasing the stiffness of the interface, they basically move toward the supports, and the sets with $K_n = K_t = 0.1, 1$ N/mm^3 result as the best approximations.

$K_n = K_t = 0.1$ N/mm^3

$K_n = K_t = 1$ N/mm^3

$K_n = K_t = 10$ N/mm^3
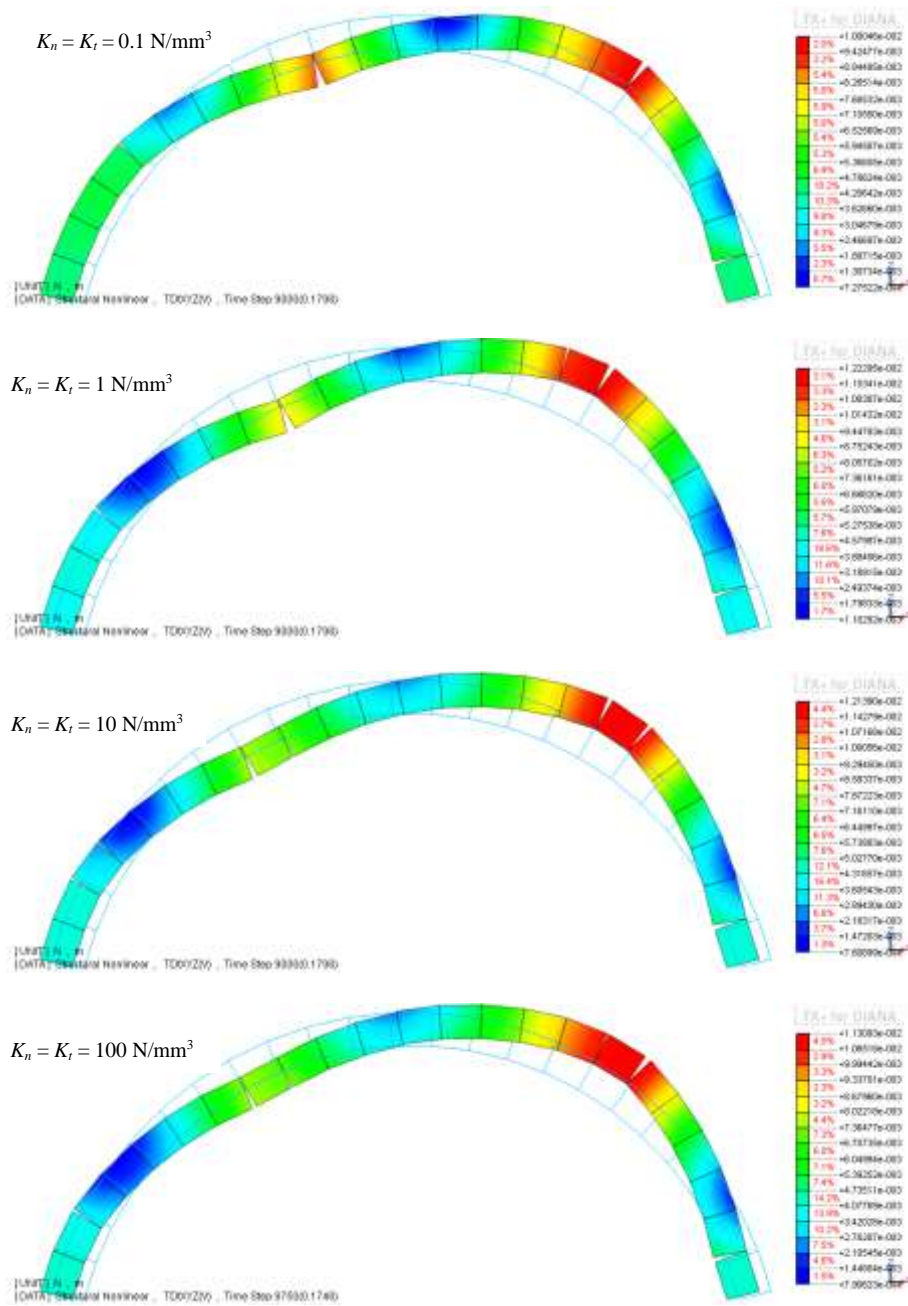
$K_n = K_t = 100$ N/mm^3
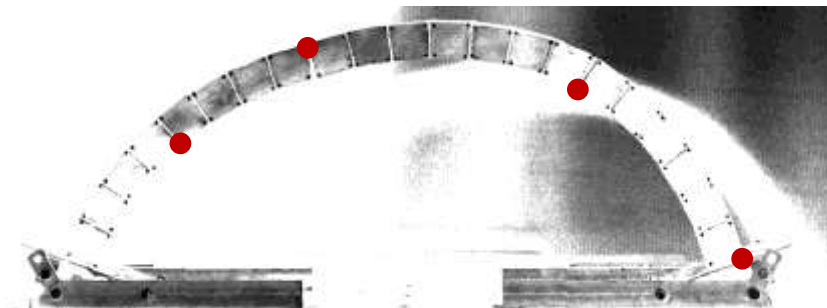
Fig. 12 Comparison between experimental test and numerical analyses with different interface properties

(3:1 displacement scale) for the 1.3 g and 10 Hz signal at the same instant

The numerical models were also assessed comparing the displacements relative to the slip table and the record of the feature tracking technique. Two control points were selected, namely, the extrados corners of the sixth voussoir from both springs (**Fig. 13**). The position of Control point #2 is justified by the location of hinge C of **Fig. 8**, whereas Control point #1 is simply the symmetric one with respect to the axis of symmetry. **Fig. 14** and **Fig. 15** show the comparison inherent the signals 10 Hz - 1.3 g and 5 Hz - 0.5 g, where the displacements of the

control points are shown up to the end of the signals (0.3 and 0.6 s, respectively). As it is possible to notice, the match is notable.
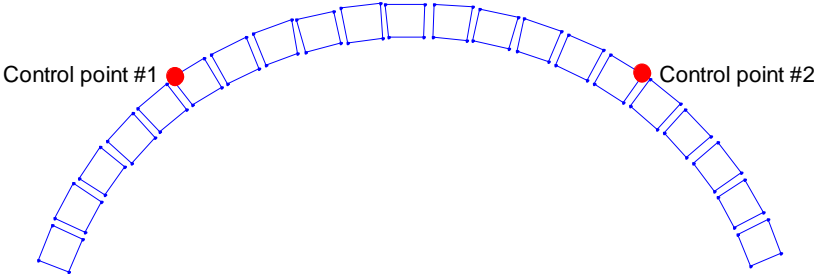

Fig. 13 Sketch of the arch voussoirs by means of marker location and position of the control points
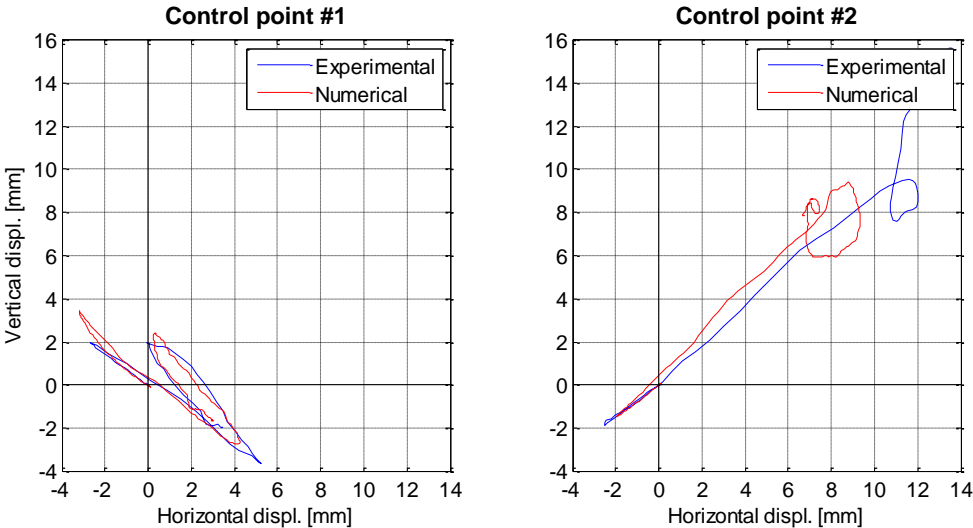

Fig. 14 Displacement of the two control points: experimental and numerical results for $Kn = Kt = 0.1$ N/mm^3
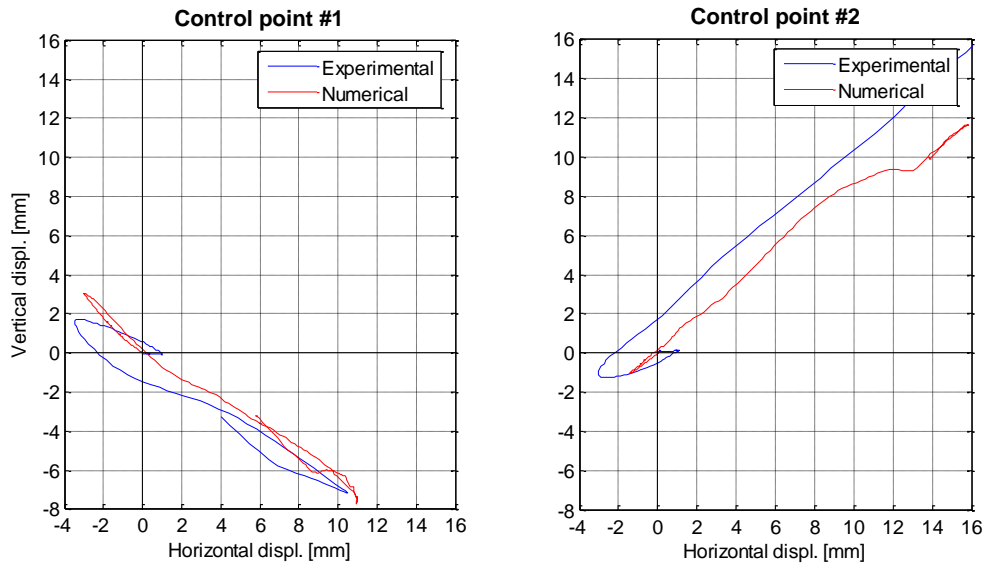(10 Hz - 1.3 g signal)

Fig. 15 Displacement of the two control points: experimental and numerical results for $Kn = Kt = 0.1$ N/mm^3
(5 Hz - 0.5 g signal)

Finally, the results of the numerical analyses, considering only the interface stiffness equal to $K_n = K_t = 0.1$ N/mm^3 are reported in **Fig. 16** (refer to **Fig. 7**). The signals recorded on the table that brought the physical arch to collapse were scaled up to achieve a failure configuration in the numerical analyses. The results matched well the experimental outcomes in the low frequency range, slightly overestimating the capacity for higher frequency values. The collapse mechanism was also well predicted by the numerical model. As an example, the deformed shape following the 1.3 g - 10 Hz signal is reported in **Fig. 17** (the lower voussoirs are fully constrained to account for the supports) together with the recorded frame of the tests.
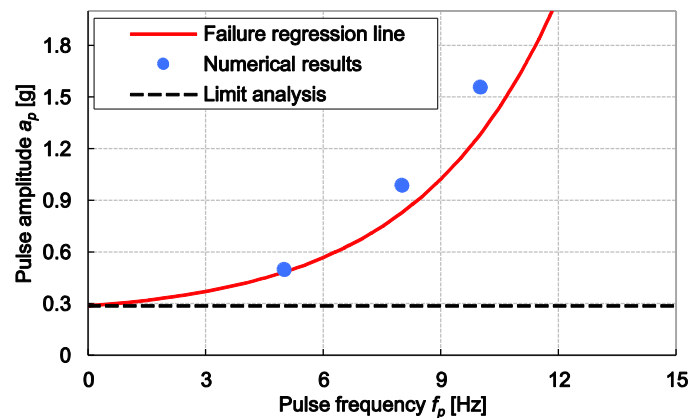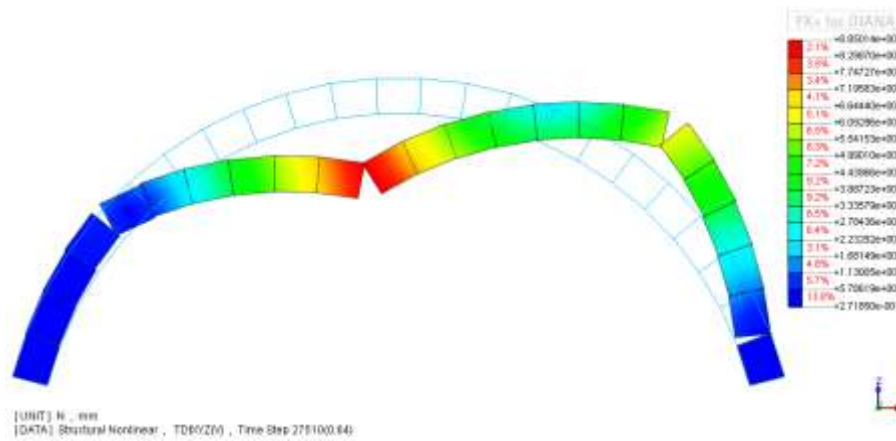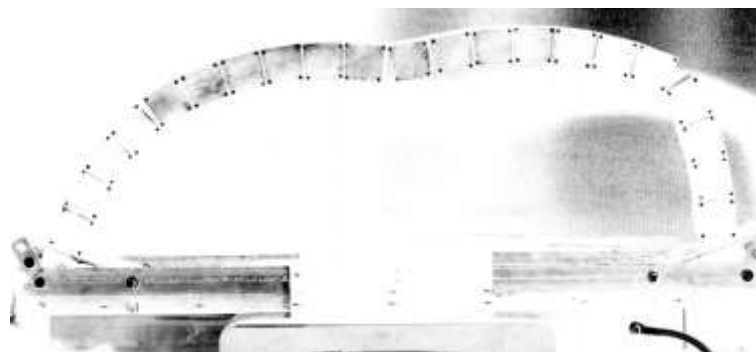

Fig. 16 Results of the numerical analyses with $K_n = K_t = 0.1$ N/mm^3

a)

b)

Fig. 17 1.3 g - 10 Hz signal ultimate displacement: comparison between

a) FEM analysis (1:1 displacement scale) and b) recorded frame of the test

Finally, additional considerations on scale effect are worth being noticed. Since the present study has dealt with (assumed) rigid blocks, the failure is a matter of stability, which does not concern the strength of the material. Accordingly, the specific mass of the specimen may be not related to the one of real structures, as in the present case, but it is still possible to get generalized results only by means of the geometrical factor π (Liberatore and Spera 2001; De Lorenzis et al. 2007; DeJong et al. 2008). In particular, regarding dynamic analysis, time and frequency are related to π through the quantity $\pi^{0.5}$ and $\pi^{-0.5}$, respectively. Consequently, considering the curve reported in **Fig. 7**, regardless the specific mass, the performance of similar arches (equal thickness/inner radius ratio and angle of embrace) can be assessed simply scaling the curve along the abscissa by the factor $\pi^{-0.5}$. As a matter of fact, discarding the possible damage due to higher energy impacts, larger arches make the curve move toward the origin, i.e. for a given impulse, frequency and shape of the arch, the capacity increases as the average radius increases (De Lorenzis et al. 2007; DeJong et al. 2008).

5. Conclusions

In the present paper, the seismic behaviour of scaled dry-joint arch was investigated under experimental tests and numerical analyses. After a preliminary tilting test, which provided data for the first calibration of the numerical model, the arch was tested under a novel signal built by a windowed three-cycle sinusoidal wave. Compared with the available literature, the specimen was subjected to the main pulse when it was not at rest, facing out-of-phase displacement. Thanks to high-speed camera, the recordings were inspected and a simplified schematization of the complex behaviour of the specimen was proposed. This schematization could represent a valuable basis for a further analytical approach. In this regard, the available literature deals only with simple shape pulses with a symmetric behaviour based on *a priori* defined mechanism. A more sophisticated model able to localize the hinges according to an energetic criterion is desirable.

The results of the shaking table tests were reported in the frequency-amplitude domain. Compared with one-cycle sine impulse, the signal adopted here resulted less conservative, that is, for a given frequency the arch can stand larger amplitude windowed pulses. This is due to the out-of-phase content which allowed the arch to, temporarily, experience unsafe displacements (coming back to a safe configuration soon after). However, in agreement with literature, the regression line that best fits the failure inputs is of exponential type.

As far as the numerical model is concerned, the major concern of this study was the implementation of FEM analyses for simulating a physical phenomenon that is basically discrete (due to dry joints). However, the model with friction interface elements (where all the nonlinearities are condensed) caught well the behaviour of the arch, even in case of large (finite) displacements. The comparison between the numerical results and the displacements recorded with a feature tracking technique showed an appreciable match.

An important conclusion for modelling is that greater attention has been paid to the stiffness of the interface elements. A sensitivity study was presented for both nonlinear static and transient analysis. For both cases, notable differences were found varying the ratio between tangential and normal stiffness (0.1, 0.4, 1). Compared with literature and experimental evidences, the smallest ratio led to unreal sliding occurrence, thus neglected. On the other hand, values equal to 0.4 and 1 provided almost coincident results.

The model calibration indicated values of normal stiffness for nonlinear static analyses valued in the range $0.1 \div 1$ N/mm^3 as the most suitable for transient analyses. However, it must be noted that these values were estimated according to a scaled specimen built with dry-joint plastic blocks, without reaching the stress levels of real scale masonry elements. This crucial aspect still requests more efforts and the behaviour of vaulted elements with different scale and materials should be investigated. It is noted that the density or stress level of the joints is

expected to affect the joint stiffness and that the stiffness of mortared joints is much larger than the stiffness values found.

Finally, regarding the nonlinear static analysis, in case geometrical nonlinearities were accounted for, a strong analogy with the nonlinear behaviour of a free-standing rigid block undergoing incremental horizontal force was stressed. Further investigations are still requested to examine in depth this aspect.

References

Al Shawa O, de Felice G, Mauro A, Sorrentino L (2012) Out-of-plane seismic behaviour of rocking masonry walls. Earthq Eng Struct Dyn 41:949–968. doi: 10.1002/eqe.1168

Albuerne A, Williams M (2015) Monitoring the seismic response of arch models using particle image velocimetry. In: SECED 2015: Earthquake Risk and Engineering towards a Resilient World. Cambridge, UK,

Albuerne A, Williams M, Lawson V (2013) Prediction of the failure mechanism of arches under base motion using DEM based on the NSCD method. Wiadomości Konserw - J Herit Conserv 34:41–47.

Alexakis H, Makris N (2014) Limit equilibrium analysis and the minimum thickness of circular masonry arches to withstand lateral inertial loading. Arch Appl Mech 84:757–772. doi: 10.1007/s00419-014-0831-4

Calderini C, Lagomarsino S (2015) Seismic response of masonry arches reinforced by tie-rods: static tests on a scale model. J Struct Eng 141:4014137–1. doi: 10.1061/(ASCE)ST.1943-541X.0001079

Calderini C, Lagomarsino S, Rossi M, et al (2015) Shaking table tests of an arch-pillars system and design of strengthening by the use of tie-rods. Bull Earthq Eng 13:279–297. doi: 10.1007/s10518-014-9678-x

Clemente P (1998) Introduction to dynamics of stone arches. Earthq Eng Struct Dyn 27:513–522. doi: 10.1002/(SICI)1096-9845(199805)27:5<513::AID-EQE740>3.0.CO;2-O

Clemente P (1997) La verifica degli archi a conci lapidei. ENEA, Unità comunicazione e informazione

D'Ayala D, Tomasoni E (2011) Three-dimensional analysis of masonry vaults using limit state analysis with finite friction. Int J Archit Herit 5:140–171. doi: 10.1080/15583050903367595

da Porto F, Tecchio G, Zampieri P, et al (2016) Simplified seismic assessment of railway masonry arch bridges by limit analysis. Struct Infrastruct Eng 12:567–591. doi: 10.1080/15732479.2015.1031141

de Felice G (2011) Out-of-plane seismic capacity of masonry depending on wall section morphology. Int J Archit Herit 5:466–482. doi: 10.1080/15583058.2010.530339

De Lorenzis L, DeJong M, Ochsendorf J (2007) Failure of masonry arches under impulse base motion. Earthq Eng Struct Dyn 36:2119–2136. doi: 10.1002/eqe.719

De Luca A, Giordano A, Mele E (2004) A simplified procedure for assessing the seismic capacity of masonry arches. Eng Struct 26:1915–1929. doi: 10.1016/j.engstruct.2004.07.003

De Santis S, de Felice G (2014) A fibre beam-based approach for the evaluation of the seismic capacity of masonry arches. Earthq Eng Struct Dyn 43:1661–1681. doi: 10.1002/eqe.2416

DeJong M (2009) Seismic assessment strategies for masonry structures. PhD dissertation, Massachusetts Institute of Technology

DeJong M (2012) Amplification of Rocking Due to Horizontal Ground Motion. Earthq Spectra 28:1405–1421. doi: 10.1193/1.4000085

DeJong M, De Lorenzis L, Adams S, Ochsendorf J (2008) Rocking stability of masonry arches in seismic regions. Earthq Spectra 24:847–865. doi: 10.1193/1.2985763

DeJong M, Dimitrakopoulos EG (2014) Dynamically equivalent rocking structures. Earthq Eng Struct Dyn 43:1543–1563. doi: 10.1002/eqe.2410

DeJong M, Ochsendorf J (2006) Analysis of vaulted masonry structures subjected to horizontal ground motion. In: Lourenco PB, Roca P, Modena C, Agrawal S (eds) 5th International Conference on Structural Analysis of Historical Constructions. New Delhi, India, pp 973–980

DeJong M, Ochsendorf J (2010) Dynamics of in-plane arch rocking: an energy approach. Proc Inst Civ Eng - Eng Comput Mech 163:179–186. doi: 10.1680/eacm.2010.163.3.179

Dimitri R, De Lorenzis L, Zavarise G (2011) Numerical study on the dynamic behavior of masonry columns and arches on buttresses with the discrete element method. Eng Struct 33:3172–3188. doi: 10.1016/j.engstruct.2011.08.018

Dimitri R, Tornabene F (2015) A parametric investigation of the seismic capacity for masonry arches and portals of different shapes. Eng Fail Anal 52:1–34. doi: 10.1016/j.engfailanal.2015.02.021

Doherty K, Griffith MC, Lam N, Wilson J (2002) Displacement-based seismic analysis for out-of-plane bending of unreinforced masonry walls. Earthq Eng Struct Dyn 31:833–850. doi: 10.1002/eqe.126

Drosopoulos GA, Stavroulakis GE, Massalas CV (2006) Limit analysis of a single span masonry bridge with unilateral frictional contact interfaces. Eng Struct 28:1864–1873. doi: 10.1016/j.engstruct.2006.03.016

Giamundo V, Lignola GP, Maddaloni G, et al (2016) Shaking table tests on a full-scale unreinforced and IMG-retrofitted clay brick masonry barrel vault. Bull Earthq Eng 14:1663–1693. doi: 10.1007/s10518-016-9886-7

Giamundo V, Lignola GP, Maddaloni G, et al (2015) Experimental investigation of the seismic performances of IMG reinforcement on curved masonry elements. Compos Part B Eng 70:53–63. doi: 10.1016/j.compositesb.2014.10.039

Griffith MC, Lam NTK, Wilson JL, Doherty K (2004) Experimental investigation of unreinforced brick masonry walls in flexure. J Struct Eng 130:423–432. doi: 10.1061/(ASCE)0733-9445(2004)130:3(423)

Griffith MC, Magenes G, Melis G, Picchi L (2003) Evaluation of out-of-plane stability of unreinforced masonry walls subjected to seismic excitation. J Earthq Eng 7:141–169. doi: 10.1080/13632460309350476

Hilber HM, Hughes TJR, Taylor RL (1977) Improved numerical dissipation for time integration algorithms in structural dynamics. Earthq Eng Struct Dyn 5:283–292. doi: 10.1002/eqe.4290050306

Housner GW (1963) The behavior of inverted pendulum structures during earthquakes. Bull Seismol Soc Am 53:403–417.

Kalkan E, Kunnath SK (2006) Effects of Fling Step and Forward Directivity on Seismic Response of Buildings. Earthq Spectra 22:367–390. doi: 10.1193/1.2192560

Lancioni G, Gentilucci D, Quagliarini E, Lenci S (2016) Seismic vulnerability of ancient stone arches by using a numerical model based on the Non-Smooth Contact Dynamics method. Eng Struct 119:110–121. doi: 10.1016/j.engstruct.2016.04.001

Lemos JV (1998) Discrete element modelling of the seismic behaviour of stone masonry arches. In: Pande GN, Middleton J, Kralj B (eds) Fourth International Symposium on Computer Methods in Structural Masonry. E & FN Spon, London, UK, pp 220–227

Liberatore D, Larotonda A, Dolce M (1997) Analisi dinamica di archi in conci lapidei soggetti ad azioni sismiche. In: 2nd National conference "Il patrimonio culturale e la questione sismica." Rome, pp 551–571

Liberatore D, Spera G (2001) Response of slender blocks subjected to seismic motion of the base: Experimental results and numerical analyses. In: Hughes TG, Pande GN (eds) 5th Int. Symposium on Computer Methods in Structural Masonry. Rome, pp 117–124

Lourenço PB (1996) Computational strategies for masonry structures. PhD dissertation, Delft University of Technology

Lourenço PB, Hunegn T, Medeiros P, Peixinho N (2010) Testing and analysis of masonry arches subjected to impact loads. In: 6th International Conference on Arch Bridges. Fuzhou, China, pp 603–610

Milani G, Lourenço PB (2012) 3D non-linear behavior of masonry arch bridges. Comput Struct 110–111:133–150. doi: 10.1016/j.compstruc.2012.07.008

Monti G, Vailati M, Gaetani A, Paolone A (2013) Modelli analitici di capacità per archi di muratura rinforzati soggetti ad azioni sismiche. In: ANIDIS 2013 - L'ingegneria sismica in Italia. Padua, p 8

Moroni M, Cenedese A (2015) Laboratory Simulations of Local Winds in the Atmospheric Boundary Layer via Image Analysis. Adv Meteorol 2015:1–34. doi: 10.1155/2015/618903

Moroni M, Cenedese A (2005) Comparison among feature tracking and more consolidated velocimetry image analysis techniques in a fully developed turbulent channel flow. Meas Sci Technol 16:2307–2322. doi: 10.1088/0957-0233/16/11/025

National Civil Protection Service (2013) Manuale per la compilazione della scheda per il rilievo del danno ai beni culturali, chiese - MODELLO A-DC. Ed. by Simona Papa and Giacomo Di Pasquale

Oppenheim IJ (1992) The masonry arch as a four-link mechanism under base motion. Earthq Eng Struct Dyn 21:1005–1017. doi: 10.1002/eqe.4290211105

Pelà L, Aprile A, Benedetti A (2009) Seismic assessment of masonry arch bridges. Eng Struct 31:1777–1788. doi: 10.1016/j.engstruct.2009.02.012

Peña F, Lourenço PB, Lemos J V. (2006) Modeling the dynamic behaviour of masonry walls as rigid blocks.

Pérez-Aparicio JL, Bravo R, Ortiz P (2013) Refined element discontinuous numerical analysis of dry-contact masonry arches. Eng Struct 48:578–587. doi: 10.1016/j.engstruct.2012.09.027

Ptaszkowska J, Oliveira D (2014) Numerical modeling of masonry vaults strengthened with transversal diaphragms. In: F. Peña and M. Chávez (ed) SAHC2014 - 9th International Conference on Structural Analysis of Historical Constructions. Mexico City, Mexico,

Rafiee A, Vinches M (2013) Mechanical behaviour of a stone masonry bridge assessed using an implicit discrete element method. Eng Struct 48:739–749. doi: 10.1016/j.engstruct.2012.11.035

Rafiee A, Vinches M, Bohatier C (2008) Application of the NSCD method to analyse the dynamic behaviour of stone arched structures. Int J Solids Struct 45:6269–6283. doi: 10.1016/j.ijsolstr.2008.07.034

Rossi M, Calderini C, Lagomarsino S, Milani G (2014) Seismic response of masonry vaulted structures : experimental and numerical modelling. In: Lourenço PB, Haseltine BA, Vasconcelos G (eds) 9th International Masonry Conference. Universidade do Minho, Guimarães,

Senthivel R, Lourenço PB (2009) Finite element modelling of deformation characteristics of historical stone masonry shear walls. Eng Struct 31:1930–1943. doi: 10.1016/j.engstruct.2009.02.046

Shindler L, Moroni M, Cenedese A (2012) Using optical flow equation for particle detection and velocity prediction in particle tracking. Appl Math Comput 218:8684–8694. doi: 10.1016/j.amc.2012.02.030

Tecchio G, Donà M, da Porto F (2016) Seismic fragility curves of as-built single-span masonry arch bridges. Bull Earthq Eng. doi: 10.1007/s10518-016-9931-6

Thavalingam A, Bicanic N, Robinson JI, Ponniah DA (2001) Computational framework for discontinuous modelling of masonry arch bridges. Comput Struct 79:1821–1830. doi: 10.1016/S0045-7949(01)00102-X

TNO DIANA BV (2014) DIANA finite element analysis; User's manual release 9.6. TNO DIANA BV, Delft

Tóth AR, Orbán Z, Bagi K (2009) Discrete element analysis of a stone masonry arch. Mech Res Commun 36:469–480. doi: 10.1016/j.mechrescom.2009.01.001

Zhang J, Makris N (2001) Rocking response of free-standing blocks under cycloidal pulses. J Eng Mech 127:473–483. doi: 10.1061/(ASCE)0733-9399(2001)127:5(473)

List of figures

Fig. 1 The SDOF mechanism for an arch under base excitation: a) first half cycle, b) recovering and impact, c) second half cycle

Fig. 2 Geometrical dimensions of the tested arch

Fig. 3 Experimental setup

Fig. 4 Arch mechanism following horizontal actions: a) schematic view and b) frame of the tilting test

Fig. 5 1.3 g, 10 Hz pre- and post-windowed signal (dash-dot blue line and black solid line, respectively)

Fig. 6 1.3 g, 10 Hz signal: comparison between input signal (drive) and recorded signal (dot black line and red solid line, respectively)

Fig. 7 Results of the shaking table tests

Fig. 8 Schematic description of initial (full circles) and final hinge location (dashed line). Hinges C and D do not experience significant change of location, and coincide in full and dashed circles.

Fig. 9 Arch capacity curves varying the interface stiffness [N/mm^3], with geometrical nonlinearities UL

Fig. 10 Hinge location for: a) $K_n = K_t = 0.1$ N/mm^3, and b) $K_n = K_t = 10$ N/mm^3

Fig. 11 Time history recorded on the slip table: pre- and post-filtering for the 1.3 g and 10 Hz signal (red dot line and solid black line, respectively)

Fig. 12 Sketch of the arch voussoirs by means of marker location and position of the control points

Fig. 12 Displacement of the two control points: experimental and numerical results for $Kn = Kt = 0.1$ N/mm^3

Fig. 13 Displacement of the two control points: experimental and numerical results for $Kn = Kt = 0.1$ N/mm^3 (5 Hz - 0.5 g signal)

Fig. 14 Results of the numerical analyses with $K_n = K_t = 0.1$ N/mm^3

Fig. 15 1.3 g - 10 Hz signal ultimate displacement: comparison between a) FEM analysis (1:1 displacement scale) and b) recorded frame of the test

List of tables